

Self-Assembled Asperities for Pressure-Tunable Adhesion

Naomi Deneke, Jamie A. Booth, Edwin P. Chan, and Chelsea S. Davis*

Control of adhesion is important in a host of applications including soft robotics, pick-and-place manufacturing, wearable devices, and transfer printing. While there are adhesive systems with discrete switchability between states of high and low adhesion, achieving continuously variable adhesion strength remains a challenge. In this work, a pressure-tunable adhesive (PTA) that is based on the self-assembly of stiff microscale asperities on an elastomeric substrate is presented. It is demonstrated that the adhesion strength of the PTA increases with the applied compressive preload due to the unique contact formation mechanism caused by the asperities. Additionally, a contact mechanics model is developed to explain the resulting trends. For a specific PTA design, the critical pull-off force can be increased from 0.4 to 30 mN by increasing the applied preload from 1 to 30 mN. Finally, the applicability of precision control of adhesion strength is demonstrated by utilizing the PTA for pick-and-place material handling. The approach in pressure-tunable adhesive design based on self-assembly of asperities presents a scalable and versatile approach that is applicable to a variety of material systems having different mechanical or surface properties.

and medical devices^[4] that must be removed from skin without causing pain. Additionally, many of these applications involve adhesion to nonplanar surfaces that span large areas, implying that scalability is another requirement. Conventional pressure sensitive adhesives (PSAs) satisfy the first requirement. They can sustain large loads due to their ability to flow and establish conformal contact without significant applied pressure.^[5] While PSAs require a relatively low threshold pressure for contact formation, there is little to no change in their adhesive response if the applied pressure is above this threshold. These materials are far from ideal as large deformations are required for interfacial separation and, if the adhesive fails cohesively, permanent damage of the interface will limit its reusability and contaminate the target substrate.

Significant advances have been made in the development of new adhesive systems.

Surface modification, such as patterning with microscopic wrinkles^[6–8] or fibrillar posts,^[9–12] have been demonstrated to enhance adhesion strength or release with some success. These materials are advantageous as they can be designed with stiffer and more elastic properties relative to PSAs, which can yield switchable^[11,12] or even tunable adhesives.^[8] However, these surface modification approaches remain limited either by scalability or the inability to be adapted to a diverse range of surface chemistries. A scalable and universal strategy, which enables the modification of any adhesive surface for pressure-tunable adhesion and easy release on a variety of substrate materials and geometries, has yet to be realized. Previously,^[13] we presented a new and generalized approach to obtain a material with pressure-tunable adhesion. This new pressure-tunable adhesive (PTA) is a surface patterned material that utilizes polymer thin film dewetting. This phenomenon can be realized in a host of materials, which we leverage here to form self-assembled stiff asperities on an elastomeric substrate to control adhesion. In the present work, we study the adhesive properties of these materials and demonstrate the control of their pressure-tunable behavior by changing the size of the stiff asperities. As thin film dewetting can be designed to occur in various materials systems, we anticipate that our present strategy to generate a patterned adhesive can displace existing surface patterning approaches and be applied over large surface areas.

Polymer thin film dewetting is an interfacial phenomenon associated with an energetically favorable breakdown of a polymer film into droplets due to an external thermodynamic driving force such as temperature or solvent annealing.^[14]

1. Introduction

An ideal reversible adhesive requires the optimization of many performance requirements. It must be able to adhere to a surface and prevent separation when supporting a specified load. Yet it is also desirable to be easily detached on demand, for example in pick-and-place applications where sensitive components^[1,2] must be released without damage, or for wearable^[3]

N. Deneke, C. S. Davis
School of Materials Engineering
Purdue University
West Lafayette, Indiana 47906, USA
E-mail: chelsea@purdue.edu

J. A. Booth
Department of Mechanical Engineering
California State University Northridge
Northridge, CA 91330, USA

E. P. Chan
Material Science and Engineering Division
National Institute of Standards and Technology
Gaithersburg, MD 20899, USA

 The ORCID identification number(s) for the author(s) of this article can be found under <https://doi.org/10.1002/adma.202207337>.

© 2022 The Authors. Advanced Materials published by Wiley-VCH GmbH. This is an open access article under the terms of the Creative Commons Attribution-NonCommercial-NoDerivs License, which permits use and distribution in any medium, provided the original work is properly cited, the use is non-commercial and no modifications or adaptations are made.

DOI: 10.1002/adma.202207337

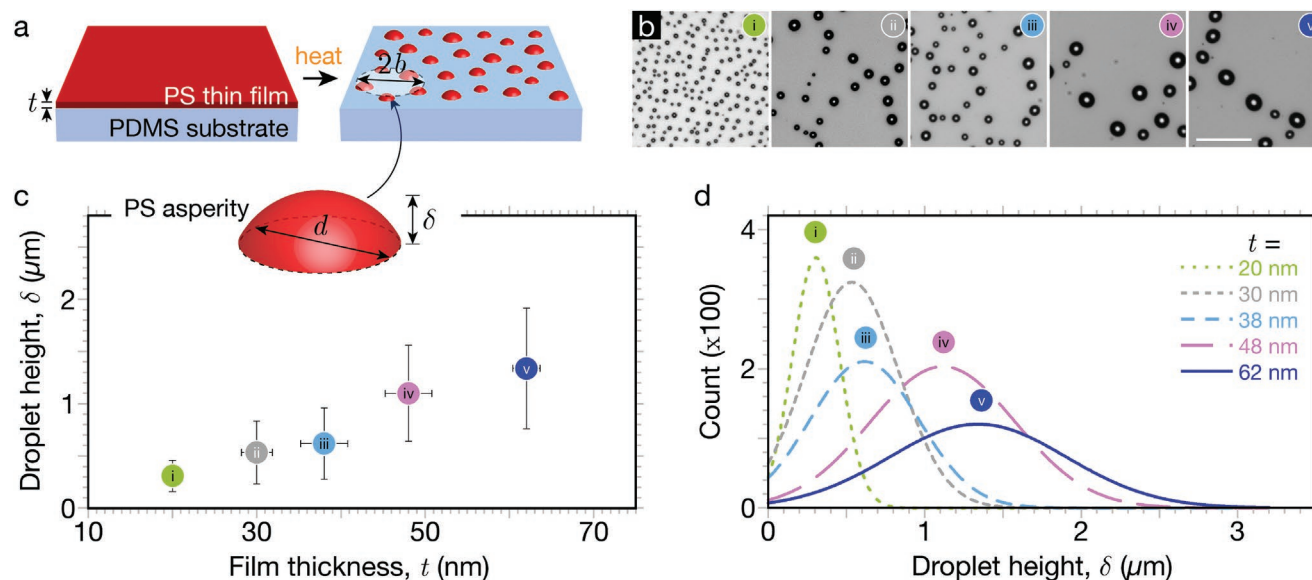


Figure 1. a) Schematic oblique view of the PTA surface before and after thermal annealing. The PS thin film, prior to annealing, has thickness, t . After annealing, the geometry is characterized by the asperity height, δ , asperity diameter, d , and polygonal cell radius, b ; b) Optical images of PTA surfaces prepared using different film thicknesses. The scale bar is $20\ \mu\text{m}$ and applies to all the images. c) Droplet height plotted as a function of film thickness. The average asperity height increases with film thickness with error bars representing one standard deviation. d) Fitted distribution curves of each asperity height on the respective PTA surface. Increasing the film thickness results in larger asperity height averages and an increased distribution in size. $n = 675, 1210, 913, 1181, 854$ for $t = 20, 30, 38, 48,$ and $62\ \text{nm}$ in (c) and (d).

Dewetting can occur during thermal annealing of a polymer film above its glass transition temperature (T_g) when there is a mismatch in the surface energies between the polymer film and the substrate (Figure 1a).^[15,16] Specifically, the dewetting process occurs in the following sequence: 1) nucleation of holes in the liquid-like polymer film due to thermal undulations, 2) radial growth of these holes, 3) coalescence of holes to form ribbons of polymer, and 4) decay of the polymer ribbons into droplets.^[15] As shown in Figure 1b, the dewetted droplets self-assemble in a characteristic polygonal pattern, and the distance between the nucleated holes ultimately defines the size and spacing of the dewetted droplets, as well as the nearest neighbor distance and the diameter of the polygonal cells. Furthermore, the size and spacing of the droplets increase with increasing distance between the nucleated holes, l . In general, l increases as film thickness, t , increases. The topographical distribution of droplets is further impacted by the dewetting mechanism (i.e., spinodal, thermal, or heterogenous) that is dependent on film thickness. Additionally, the polymer molecular mass can also affect the droplet pattern by altering the kinetics of the dewetting process, which can produce patterns such as fingering instabilities that lead to broadening of the droplet size distribution.^[17,18] A more detailed discussion of dewetting physics is presented in the Supporting Information. Here, we focus on PTAs patterned by spinodal or thermal dewetting of a thin film, where the physics of the process are governed by intermolecular forces and the distance between nucleated holes is proportional to the square of the film thickness, $l \propto t^2$.^[16]

In this work, we present a highly tunable, scalable, and versatile PTA that is based on the self-assembly of stiff microscale asperities on an elastomeric substrate via thin film dewetting. We demonstrate that the adhesion strength of the PTA

increases with the applied maximum compressive preload due to the unique contact formation mechanism caused by the asperities.

2. Results and Discussion

To fabricate the PTAs, polystyrene (PS) and poly(dimethylsiloxane) (PDMS) were chosen as the thin film and elastomeric substrate, respectively. Once dewetting was completed, the surface features were quenched, resulting in stiff spherical cap-shaped asperities on the elastomeric substrate. The size and spacing of the asperities were controlled by adjusting the film thickness prior to thermal annealing. The advantage of this approach is that any substrate material can be patterned with stiff asperities if the effective interface potential of the film and substrate is unstable.

Next, we characterize the morphology of the asperity patterns. As illustrated in Figure 1a, we characterize the asperity patterns in terms of the asperity height, δ , asperity diameter, d , and polygonal cell radius, b . A total of five PS film thicknesses were prepared and dewetted, which yielded five distinct PTA systems. Representative optical microscopy images for each system are shown in Figure 1b. As shown in Figure 1c, increasing the film thickness increases the average asperity height after thermal annealing, with an average asperity height of $0.31, 0.54, 0.62, 1.10,$ and $1.30\ \mu\text{m}$. As shown in Figure 1d, while the height distribution of the asperities becomes broader with increasing film thickness, the average height of the droplet increases with film thickness. A distribution in size for each system is a result of the dynamics of the dewetting process,^[17] and although the size of the asperities varies with film

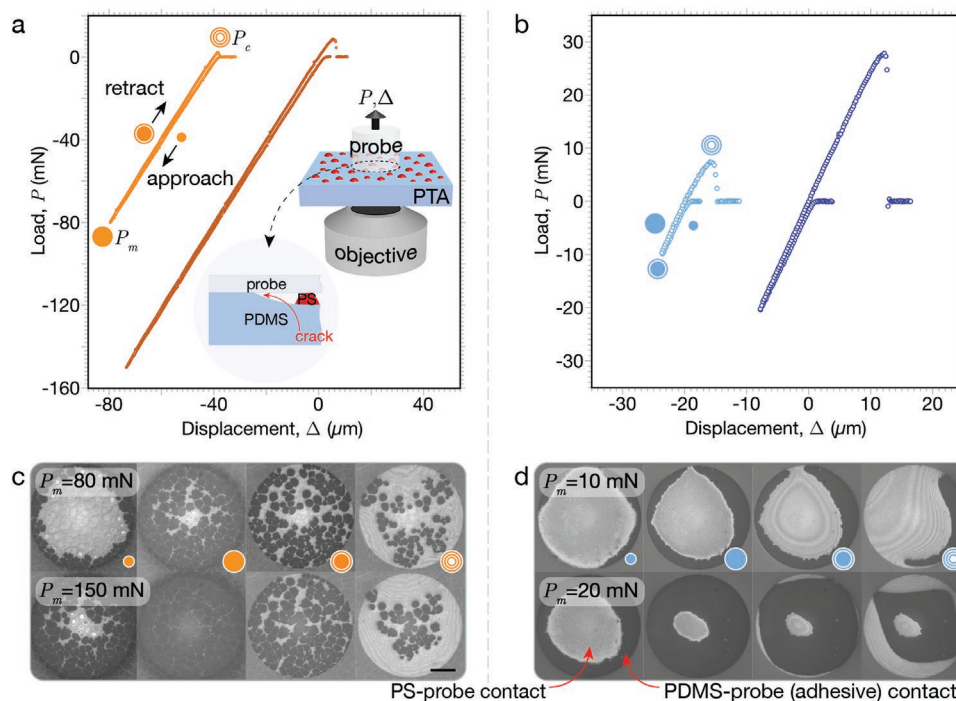


Figure 2. a) The inset shows schematic of experimental setup for contact adhesion testing. A cylindrical probe (radius 0.5 mm) is indented into the PTA surface while displacement, Δ , load, P , and contact images are gathered by the testing device. Load–displacement curves for the largest asperity height sample ($\delta = 1.30 \mu\text{m}$) are shown at two different levels of maximum compressive load; b) Load–displacement curves for the smallest asperity height sample ($\delta = 0.31 \mu\text{m}$) are shown at two different levels of maximum compressive load. The curves in (a) and (b) are offset by an arbitrary displacement value for clarity. c,d) Images of the PTA–probe interface during contact for the largest and smallest asperity height samples, respectively. The scale bar is $200 \mu\text{m}$ and applies to all the images.

thickness, they remain self-similar. A more detailed discussion of asperity self-similarity and characterization of b and d (as well as the nearest-neighbor distance between asperities, s) is provided in the Supporting Information. Having demonstrated that we can control the various geometric parameters of the asperities, we next investigate how these asperities influence the adhesion of the elastomeric substrate.

We study the effects of asperity dimensions on the adhesive performance of the PTA using contact adhesion testing.^[13,19] **Figure 2a** includes a schematic of the test, which involves bringing the flat end of a cylindrical glass probe (radius 0.5 mm) into contact with the PTA until a desired maximum compressive load, P_m , is reached. Videos of the contact adhesion tests presented in **Figure 2** can be found in the Supporting Information. The probe is then retracted from the adhesive until complete separation occurs. We use the critical pull-off load, P_c , defined as the peak tensile load achieved during retraction, as a metric to characterize the PTA's adhesive response. **Figures 2a,b** are representative adhesion testing results for PTAs with the smallest and largest asperities tested ($\delta = 0.31 \mu\text{m}$ and $\delta = 1.30 \mu\text{m}$, respectively). The profiles of the load versus displacement curves are similar between tests except for the location of P_c . This similarity in curve shape is observed across all PTA systems as shown in **Figure S4** of the Supporting Information. For both samples presented in **Figure 2**, P_c increases with increasing maximum compressive load, indicating that the adhesive response is pressure dependent. This trend in pressure dependence is consistently observed across all systems.

The effect of asperity size is evident when we observe how P_c changes as a function of P_m . **Figures 3a,b** show the tensile portion of the adhesion tests on the smallest and largest asperity PTAs, indented to different P_m values, illustrating that the size of the asperity plays an important role in controlling the critical pull-off force. The relationship between asperity size and adhesion can be more clearly resolved when we compare P_c as a function of P_m for all five PTA systems (**Figure 3c**). Each data point is based on an average P_c value for three adhesion tests at a fixed P_m . We observe that P_c increases with increasing P_m , and that smaller asperity samples can achieve higher P_c values. We also find that the pull-off force for the small asperity systems is significantly more sensitive to the applied compressive load. As asperity size increases, the PTAs strength is controlled over a broader range of compressive loads. Additionally, P_c values plateau to a maximum, signifying a point where there is little change in the adhesive response beyond a threshold P_m value. These trends can be explained by studying the global and local contact formation and separation mechanisms, both from contact videos and by performing an analysis of the contact mechanics, the details of which are discussed below.

The enhancement in P_c can be explained by studying the contact formation and separation mechanisms at both macroscopic (across the entire face of the probe) and microscopic (at local sub-contacts) length scales. We begin our analysis by observing the macroscopic contact. **Figures 2c,d** display a sequence of images of the entire PTA–probe interface during contact formation and separation for PTAs with large and

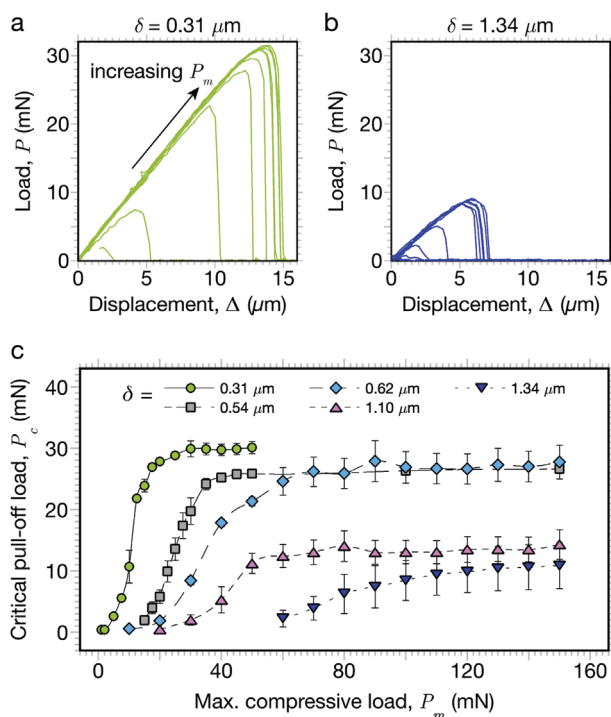


Figure 3. The tensile portion of the load–displacement curve for tests with varying maximum compressive load, performed on a) the lowest asperity height sample ($\delta = 0.31 \mu\text{m}$) and b) the highest asperity height sample ($\delta = 1.30 \mu\text{m}$). c) Pull-off load as a function of preload for PTA surfaces with varying asperity height, δ . Pressure tunability is achieved over a wider range of compressive preloads as asperity height increases, while the maximum adhesive strength is reduced. The error bars represent one standard deviation and $n = 3$ for each data point.

small asperities. The brightest regions in the images represent the area of non-adhesive contact underneath the probe, and the dark patches are adhesive contact formation between the probe and PDMS substrate. Here, we see that the contact line moves radially inward toward the center of the probe during approach and reaches the maximum interfacial contact at P_m . We attribute this mechanism of contact formation to the non-uniform stress distribution in the elastic adhesive substrate during contact.^[20] Traditionally, an instantaneous “jump-to-contact” of the elastomer to the probe is observed with non-patterned PDMS due to attractive forces drawing the two surfaces together. However, the presence of the stiff asperities prevents this from occurring, and consequently makes contact formation more pressure dependent. It is well documented that the radial pressure profile resulting from the contact of a cylindrical probe and elastic body increases from the center of the contact to the perimeter.^[20] This results in adhesive contact formation that initiates from the outer edge of the probe. When the applied preload is increased, the total contact area between the probe and the adhesive PDMS substrate increases. This effect is observed when comparing the top rows (low preload) and bottom rows (high preload) of Figure 2c,d. This larger amount of contact correlates to an increase in adhesion, as quantified by P_c . Consequently, we observe a pressure-dependent adhesive response for all PTAs, as presented in Figure 3.

While this macroscopic contact analysis explains the pressure tunability observed in all PTA systems, it does not explain differences in plateau strength and the sensitivity to applied preload between samples, highlighted in Figure 3. We can explain this difference by analyzing the contact formation and separation mechanism on the local level, i.e., at a single sub-contact. A sub-contact is considered the contact within a single cluster of asperities, as illustrated in Figure 4a. Each ring or cluster of PS asperities can effectively behave as a rigid flat-bottomed ring as shown in Figure 4b, which is an approximation that is used in our adhesion model. As the applied load increases, adhesive contact is eventually established within the interstitial spacing of the asperities. Figure 4c illustrates the cross section of the PTA-probe interface along the dashed line shown in Figure 4a,b, at four stages during contact formation and separation. First, the probe contacts the peaks of the stiff PS asperities, which leads to local indentation of the asperities into the compliant PDMS substrate. Next, at a threshold stress, the local deformation displaces the stiff asperities sufficiently, such that the probe can interact with the PDMS substrate and form an adhesive contact of radius, a . Therefore, adhesive contact formation is dependent on the applied load, as well as the density and geometry of the asperities. A larger compressive load is needed to displace larger or more closely spaced asperities into the PDMS substrate. Furthermore, increased local deformation of the elastic substrate by the stiff asperities results in more stored elastic strain energy that can aid in interfacial separation. Hence, PTAs with larger asperities have a lower adhesion response.

As the probe is retracted, a is reduced until complete separation occurs. Changes in the contact area can alternatively be viewed as the propagation of an annular crack that forms around the ring of asperities (as illustrated in Figure 4b and outlined in purple in Figure 4c). The size of the crack and the stress state at the crack tip is dependent on the applied load, the substrate stiffness, and the asperity size. When we visualize the adhesive failure during adhesion testing (Figure 2c), crack propagation is initially localized at the perimeter of polygonal cells across the interface for the PTA with larger asperities, whereas global failure occurs along the perimeter of the probe for the PTA with smaller asperities. This difference suggests that there is an interplay between global stresses across the interface that arise due to external loading by the probe and local stresses at each cluster of asperities that are dependent upon the asperity size and spacing.

To aid in our understanding of the adhesive response as a function of the geometric parameters that can be controlled in our PTAs, we construct an adhesion model based on linear elastic fracture mechanics. Having observed that contact between the probe and PDMS substrate occurs within rings of asperities, our model focuses on understanding the local behavior of a single sub-contact as schematically depicted in Figure 5a. The shape of the PS asperity is assumed to be a spherical cap, with the asperity and PDMS substrate interface considered flat. For simplicity, we assume that the contact formed between the probe and the substrate is axisymmetric, the contact area of this local contact is defined by radius a , and the perimeter of a single sub-contact is a rigid ring of inner radius b . We assume that a crack is always present such

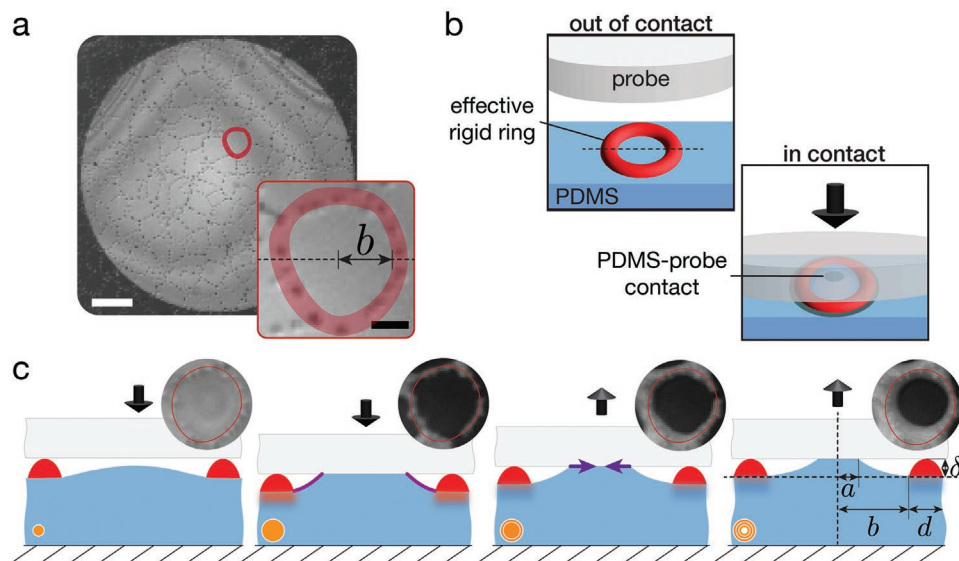


Figure 4. a) Exemplary sub-contact formation in the interstitial spacing of a cluster of asperities on the largest asperity height sample ($\delta = 1.30 \mu\text{m}$). The perimeter of the region, highlighted in red, is composed of the PS asperities. The white scale bar is $150 \mu\text{m}$ and the black scale bar (inset) is $30 \mu\text{m}$. b) Schematic illustrating an oblique view of the PTA and probe before and after adhesive contact is formed. The cluster of PS asperities effectively behave as a rigid ring, in the center of which a contact forms between the PDMS and the probe. The dashed lines in (a) and (b) indicate the lateral location taken for the cross-section of the contact during formation and separation. The orange circular labels illustrate the correlation with P values highlighted in Figure 2a. The insets show experimental contact images of the region highlighted in (a) during the approach and retraction phases of an adhesion test and have a physical diameter of approximately $100 \mu\text{m}$.

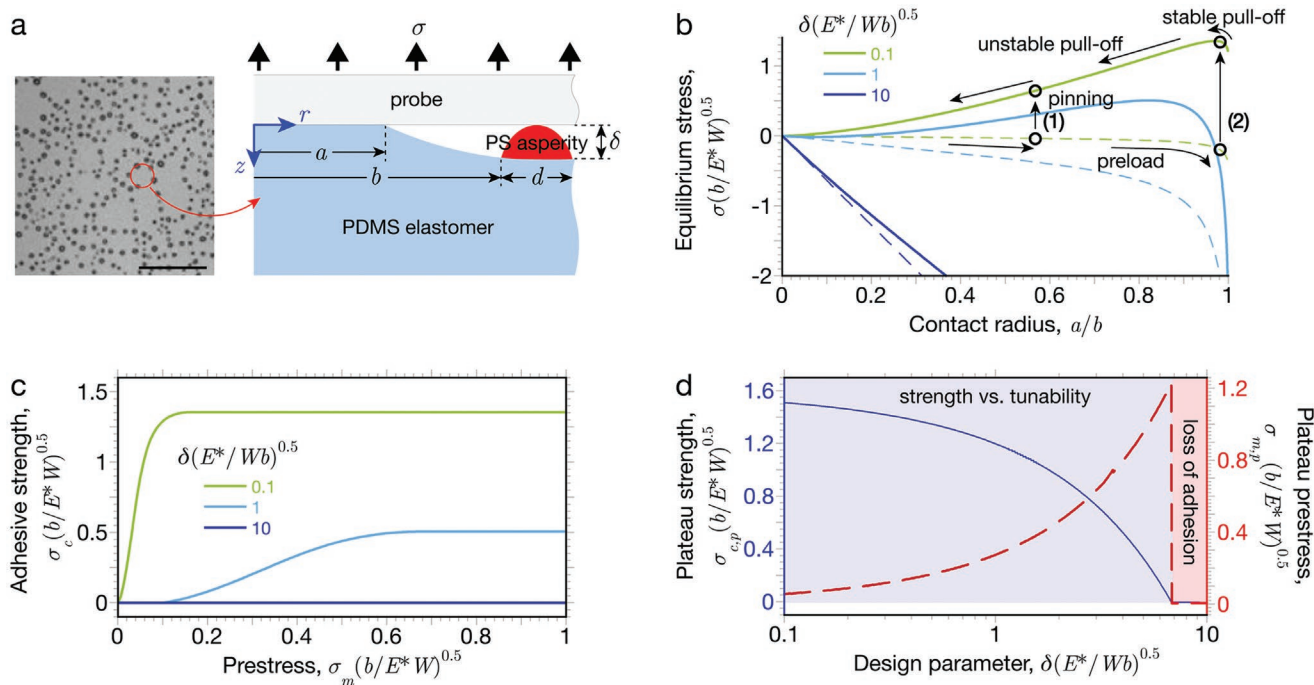


Figure 5. a) Schematic of the axisymmetric contact at an individual cluster of asperities. b) Dimensionless equilibrium stress, $\sigma \sqrt{b/E^*W}$, as a function of dimensionless contact radius, a/b . Both the adhesive (solid line, Equation 3) and non-adhesive (dashed line, Equation 4) forms are shown. Results for three values of the dimensionless design parameter, $\delta \sqrt{E^*/Wb}$, are presented. In all cases, the dimensionless asperity diameter $d/b = 0.1$. Two exemplary measurements are shown, labeled (1) and (2), assuming a non-adhesive preload. c) Dimensionless adhesive strength, $\sigma_c \sqrt{b/E^*W}$, as a function of the dimensionless prestress, $\sigma_m \sqrt{b/E^*W}$. d) A design map that illustrates the reduction in plateau strength and increase in plateau prestress as the dimensionless design parameter, $\delta \sqrt{E^*/Wb}$, increases until there is total loss in adhesion.

that a is always smaller than b , $a < b$. The width and height of this ring are equivalent to the asperity diameter d , and height, δ , respectively. The PTA substrate is treated as an elastic half-space, and the contact with the probe is assumed to be frictionless. The circumference of the contacting region behaves as the tip of an annular crack. This crack is effectively loaded by the opening displacement imposed by the asperity height. It is also loaded by the remote stress, σ , applied to the contact by the probe.

Under this set of assumptions, the stress intensity factor (K_I) at the crack tip can be obtained by the superposition of existing solutions for the two loading conditions.^[21,22] If the interface between the asperity and adhesive substrate was ideally flat and the asperity was rigid, as assumed, then it would impose a uniform normal displacement on the adhesive substrate when indented. Since no closed-form analytical solution exists for this elasticity problem, and the true shape of this interface is unknown, the assumption of a uniform pressure distribution exerted on the elastomer surface under the asperity is made instead. A closed-form solution is available for this problem leading to the stress intensity factor^[21,22]

$$K_I = \frac{\sigma \pi b^2}{2a\sqrt{\pi a}} + \frac{\delta E^*}{\sqrt{\pi a}} f\left(\frac{a}{b}, \frac{d}{b}\right) \quad (1)$$

where the plane strain modulus is $E^* = E/(1 - \nu^2)$. The function f describes a dimensionless quantity that is geometry dependent, and the full solution of f , along with the detailed derivation of Equation (1), is provided in the Supporting Information. The critical value of the stress intensity factor where interfacial separation occurs is related to the energy requirement of this separation, the work of adhesion W , via the Irwin relationship^[23]

$$K_c = \sqrt{2E^*W} \quad (2)$$

Combining Equation (1) and Equation (2), we obtain the equilibrium stress as

$$\sigma \sqrt{\frac{b}{E^*W}} = \sqrt{\frac{8}{\pi} \left(\frac{a}{b}\right)^3} - \frac{2}{\pi} \left(\delta \sqrt{\frac{E^*}{Wb}} \right) \frac{a}{b} f\left(\frac{a}{b}, \frac{d}{b}\right) \quad (3)$$

where the parameters are arranged in dimensionless groups. It is also useful to consider the equilibrium stress when the interface is non-adhesive ($W = 0$). In terms of the same dimensionless groups, the result is

$$\sigma \sqrt{\frac{b}{E^*W}} = -\frac{2}{\pi} \left(\delta \sqrt{\frac{E^*}{Wb}} \right) \frac{a}{b} f\left(\frac{a}{b}, \frac{d}{b}\right) \quad (4)$$

Figure 5b shows the results of both Equation (3) and Equation (4), for multiple values of the dimensionless parameter, $\tilde{\delta} = \delta(E^*/Wb)^{0.5}$. We consider $\tilde{\delta}$ to be the design parameter since the characteristic asperity height (δ), cluster radius (b), elastic modulus (E^*), and work of adhesion (W), can be separately controlled in our experimental design. In all cases presented in Figure 5, the dimensionless asperity diameter $\tilde{d} = d/b = 0.1$. Examining the smallest value of the design parameter ($\tilde{\delta} = 0.1$), representing small asperities

spaced far apart on a compliant substrate and with a strong adhesive interaction, we observe only compressive (negative) equilibrium stresses in the non-adhesive case (green dashed line in Figure 5b, Equation 4). The contact radius grows as the magnitude of this compressive stress is increased. In the adhesive case (green solid line in Figure 5b, Equation 3), tensile (positive) equilibrium stresses are possible. A maximum in the tensile stress is observed at an intermediate value of the contact radius. As the design parameter is increased to $\tilde{\delta} = 1$, representing larger asperities with smaller spacing on a less compliant substrate and weaker adhesive interaction, a larger magnitude of compressive stress is required to form the contact. In the adhesive case, tensile equilibrium stresses are observed over a smaller range of contact radii, and with a lower maximum stress. Eventually, in the case of $\tilde{\delta} = 10$, tensile equilibrium stresses are no longer observed. This result implies that the surface has lost the capability to bear load despite adhesive interaction being present.

The insights gained from the predictions of our model reveal the source of the preload dependence and plateau of the adhesive strength in the PTA, which is consistent with the experimental results shown in Figure 3. Interfacial interactions typically exhibit hysteresis,^[19] meaning that the distance over which surfaces jump out of plane to form a contact is much smaller than the corresponding displacement required to achieve separation. We proceed under the assumption that we can treat the approach and subsequent contact formation as non-adhesive, an approach previously utilized when considering preload dependence in the presence of contact curvature.^[24] For this reason, during approach we move along the non-adhesive stress curve until a specified compressive prestress is reached. Figure 5b shows two representative cases with different magnitudes of prestress. In case (1), the contact grows to a specific radius that is a function of the prestress. As the surfaces are then retracted, the contact line becomes pinned due to the presence of adhesion. As the applied stress becomes tensile, the contact only changes size once the equilibrium adhesive stress is reached. At this point, since the equilibrium adhesive stress is reduced with decreasing contact radius, the pull-off strength (defined as the maximum tensile stress observed during approach and retraction) is observed at the point the contact begins to shrink. If the compressive prestress is increased further, the pull-off strength will grow. This continues until the tensile equilibrium adhesive stress attains its maximum value. Case (2) illustrates the behavior beyond this point, at increasingly larger compressive prestresses. At the point of pinning, a reduction in the contact radius requires an increase in the tensile stress. This leads to a regime where the crack propagates in a stable manner until the maximum tensile stress is attained, at which point separation once again becomes unstable.

Figure 5c shows the dimensionless pull-off strength as a function of the prestress (also in dimensionless form). The same values of the dimensionless design parameter are considered here. The plateau in Figure 5c emphasizes that prestressing beyond the point of the maximum tensile stress (as in case (2) of Figure 5b) does not increase the resulting pull-off strength. As the dimensionless design parameter is increased to $\tilde{\delta} = 1$, the plateau occurs at a higher prestress and with a lower pull-off

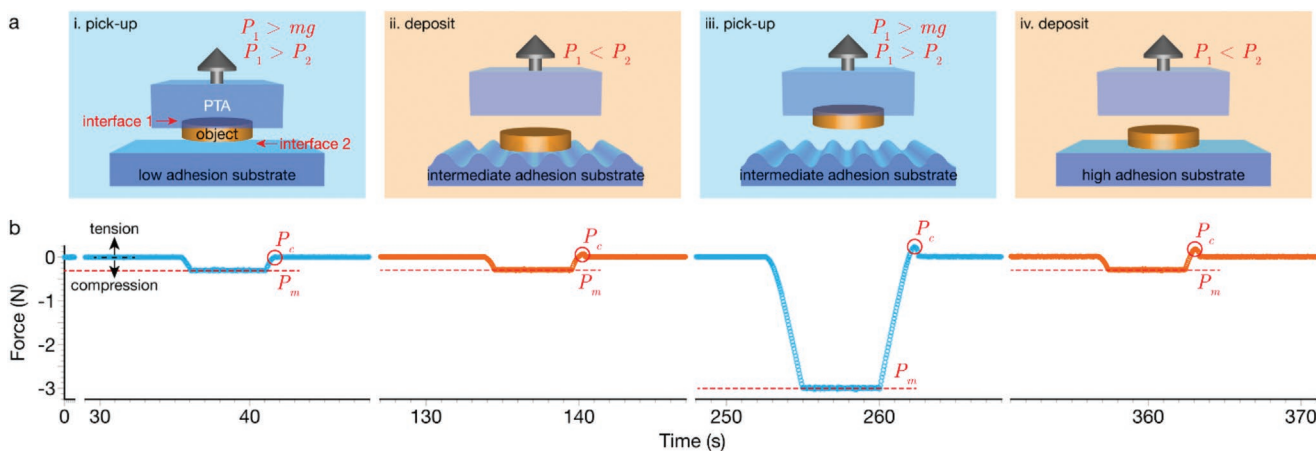


Figure 6. Demonstration of the pick-and-place capabilities of the PTA. a) The PTA picks up and deposits a circular disk from three consecutive substrates that have increasingly greater adhesive properties from left to right. b) The load during pick-up and deposition of the substrate as a function of time. Careful tuning of the PTA adhesion strength is required to pick up the disk from the intermediate substrate by changing the amount of load applied during contact. A video of this experiment is available in the Supporting Information.

strength. In the case of $\tilde{\delta} = 10$, the pull-off strength is zero for any prestress. This provides an explanation for the behavior observed in the experimental results of Figure 3, where the pull-off force plateaus to lower values as the asperity size was increased and with a more gradual transition to the plateau value.

The relationship in Figure 5c also illustrates that there is a trade-off in performance for PTAs as the asperity design parameter is varied. A more gradual transition to the plateau strength enhances the tunability of the adhesive, as less precise control over the prestress is required, but coincides with a lower plateau strength indicating reduced load bearing capability. Figure 5c illustrates this by comparing the predictions of the dimensionless plateau strength and plateau prestress versus the asperity design parameter, $\tilde{\delta}$. Generally, larger asperities with smaller spacing, less compliant adhesive substrates, or weaker adhesive interactions have reduced ultimate adhesive strength but a greater tunability with respect to the compressive load applied during contact formation.

To demonstrate the potential of the PTA for real-world applications, such as pick-and-place material handling, we apply the PTA as a device for the transfer of a cylindrical object between multiple surfaces with different interfacial properties (Figure 6). Surfaces with increasing adhesion strengths (glass, wrinkled PDMS and smooth PDMS) are sequentially arranged in the experiment. Varying values of the compressive load, P_m , are applied during pick-up and deposition of the disk, and the adhesive strengths of the PTA-object interface and object-substrate interface are characterized as P_1 and P_2 , respectively (Figure 6a). The object is picked up from the low adhesion substrate (glass) by the PTA using a moderate preload that results in $P_1 > P_2$. The cylinder is then deposited onto the next substrate (wrinkled PDMS) using the same preload due to intermediate adhesion between the object and substrate that is greater than the adhesion between the object and PTA, hence $P_2 > P_1$. The object is then picked up from the same substrate with a larger preload, indicating that $P_1 > P_2$. Finally, the object is deposited onto the final substrate (smooth PDMS) using

the same moderate preload due to high adhesion between the object and substrate and $P_2 < P_1$. The corresponding video is provided in the Supporting Information. We show that for a given PTA system, adhesion strength is controlled by careful selection of the preload (or prestress), most notably during deposition and pick-up from the intermediate adhesion substrate.

3. Conclusion

We have developed a new form of a pressure-tunable adhesive that can achieve a range of adhesive responses. The key to the pressure-tunable response is the patterning of self-assembled stiff asperities on a compliant elastomeric substrate. The adhesion experiments show that the pull-off force increases as the amount of compressive preload is increased before reaching a plateau. We have presented an adhesion model that reveals the source of this plateau in strength is related to adhesion hysteresis during approach and retraction steps. The model also illustrates that surfaces with smaller, more broadly spaced asperities exhibit a higher adhesive strength but with reduced pressure tunability, which is in agreement with the experimental results. As we have demonstrated, the PTA has the potential to be used for pick-and-place material handling applications. Although there are numerous surface patterning approaches, the advantage of thin film dewetting is that it is scalable, as well as adaptable to any material and surface planarity, thus making it amenable to a wide variety of applications. This materials design can be further exploited by changing the mechanical or surface properties of the adhesive substrate and stiff asperities to achieve new pressure-tunable adhesion properties for more tailored control or specific engineering requirements. For instance, to enable a more robust PTA that can be cleaned and re-usable, instead of using a polymer thin film, one can use a photocurable methyl methacrylate formulation that will undergo autophobic dewetting to form droplets on the PDMS surface. The

droplets can then be subsequently photocrosslinked to form a semi-interpenetrated network with the substrate to 1) enhance interfacial strength between the droplets and the substrate and 2) prevent dissolution of the droplets when the interface needs to be cleaned.

4. Experimental Section

Certain instruments and materials are identified in this work to adequately specify the experimental details. Such identification does not imply a recommendation by the National Institute of Standards and Technology, nor does it imply that the materials are necessarily the best available for the purpose.

PTA Fabrication: To fabricate the PTA, a PS thin film dewets from a silicone elastomer to pattern the elastomer surface with stiff asperities arranged in a polygonal pattern. The size of the asperities was controlled by manipulating the thickness of the PS film. Thin films were prepared by spin coating 0.5 mass %, 0.75 mass %, 1.0 mass %, 1.2 mass %, and 1.5 mass % solutions of PS (Polymer Source, Inc.) with molecular mass = 105.5 kg mol⁻¹, polydispersity index = 1.05 in toluene (Sigma Aldrich) on a silicon wafer to obtain 20, 30, 38, 48, and 62 nm thick films, respectively. Each film was then transferred onto the surface of a bulk elastomer, PDMS (Dow Sylgard 184) using a film transfer method detailed in the previous publication.^[13] The bilayer polymer sample is thermally annealed at 160 °C (above the glass transition temperature of PS) for 24 h. The now mobile PS polymer chains dewet from the PDMS substrate to minimize surface area. The droplets arrange into a polygonal pattern that is characteristic of thin film dewetting and solidify upon quenching to leave stiff asperities on the substrate surface.

Contact Adhesion Testing: Contact adhesion testing was used to measure the PTA's adhesive response to applied load. A custom-built adhesion testing device controls the displacement of a 1 mm diameter aluminosilicate glass probe (Edmund Optics) with a piezoelectric actuator (Physik Instrumente N-381 Nexact) and the normal load on the probe was recorded with a load cell (Futek LSB200). The test was performed over a microscope to image the PTA-probe interface. The flat end of the probe was aligned with the PTA surface by positioning the probe several micrometers above the PTA and manually adjusting the pitch and yaw until Newtonian fringes in the form of concentric circles are visible. The presence of the circular Newtonian fringes signifies that the two surfaces were aligned. Tensile and compressive loads and displacements were assigned positive and negative values, respectively. The flat end of the probe indents the PTA surface at 1 μm s⁻¹ until reaching the desired maximum compressive load, P_m , and retracts at the same velocity until complete separation occurs. The P_m values selected for testing were determined by experimentally identifying the largest and smallest P_m values for which a unique P_c was observed and then selecting an appropriate P_m interval between those bounding values.

Supporting Information

Supporting Information is available from the Wiley Online Library or from the author.

Acknowledgements

The authors acknowledge Purdue University for providing financial support. N.D. acknowledges funding support from the George Washington Carver Fellowship (Grant 7100060).

Conflict of Interest

The authors declare no conflict of interest.

Data Availability Statement

The data that support the findings of this study are available from the corresponding author upon reasonable request.

Keywords

adhesion, soft mechanics, surface patterning

Received: August 11, 2022

Revised: October 19, 2022

Published online:

- [1] P. Bobka, F. Gabriel, M. Römer, T. Engbers, M. Willgeroth, K. Dröder, in *Production at the Leading Edge of Technology: Proc. 9th Congress of the German Academic Association for Production Technology (WGP), September 30th - October 2nd, Hamburg 2019*, (Eds.: J. P. Wulfsberg, W. Hintze, B.-A. Behrens) Springer Vieweg, Berlin, Germany **2019**, p. 389.
- [2] M. R. Marks, Z. Hassan, K. Y. Cheong, *Crit. Rev. Solid State Mater. Sci.* **2015**, *40*, 251.
- [3] M. Domb, in *Wearable Devices: The Big Wave of Innovation* (Eds: N. Nasiri), IntechOpen, London, UK **2019**, Ch. 7.
- [4] I. Hwang, H. Nam Kim, M. Seong, S.-H. Lee, M. Kang, H. Yi, W. Gyu Bae, M. Kyu Kwak, H. Eui Jeong, I. Hwang, M. Seong, S. Lee, M. Kang, H. Yi, H. E. Jeong, H. N. Kim, W. G. Bae, M. K. Kwak, *Adv. Healthcare Mater.* **2018**, *7*, 1800275.
- [5] C. Creton, *MRS Bull.* **2003**, *28*, 434.
- [6] C. S. Davis, A. J. Crosby, *Soft Matter* **2011**, *7*, 5373.
- [7] E. P. Chan, E. J. Smith, R. C. Hayward, A. J. Crosby, *Adv. Mater.* **2008**, *20*, 711.
- [8] P.-C. Lin, S. Vajpayee, A. Jagota, C.-Y. Hui, S. Yang, *Soft Matter* **2008**, *4*, 1830.
- [9] M. Varenberg, A. Peressadko, S. Gorb, E. Arzt, *Appl. Phys. Lett.* **2006**, *89*, 121905.
- [10] G. Carbone, E. Pierro, S. N. Gorb, *Soft Matter* **2011**, *7*, 5545.
- [11] N. Nadermann, J. Ning, A. Jagota, C.-Y. Hui, *Langmuir* **2010**, *26*, 15464.
- [12] V. Tinnemann, E. Arzt, R. Hensel, *J. Mech. Phys. Solids* **2019**, *123*, 20.
- [13] N. Deneke, A. L. Chau, C. S. Davis, *Soft Matter* **2020**, *17*, 863.
- [14] R. Xing, C. Luo, Z. Wang, Y. Han, *Polymer (Guildf)* **2007**, *48*, 3574.
- [15] T. G. Stange, D. F. Evans, W. A. Hendrickson, *Langmuir* **1997**, *13*, 4459.
- [16] G. Reiter, *Langmuir* **1993**, *9*, 1344.
- [17] D. Peschka, S. Haefner, L. Marquant, K. Jacobs, B. Wagner, *Proc. Natl. Acad. Sci. USA* **2019**, *116*, 9275.
- [18] S.-H. Choi, B.-M. Zhang Newby, *J. Chem. Phys.* **2006**, *124*, 054702.
- [19] K. R. Shull, *Mater. Sci. Eng. R.* **2002**, *36*, 1.
- [20] J. Boussinesq, *Application Des Potentiels À l'étude de l'équilibre et Du Mouvement Des Solides Élastiques*, Gauthier-Villars, Paris, France **1885**.
- [21] H. Tada, P. C. Paris, G. R. Irwin, *The Stress Analysis of Cracks Handbook*, ASME Press, St. Louis, MO, USA **1973**.
- [22] D. Maugis, *J. Colloid Interface Sci.* **1992**, *150*, 243.
- [23] G. R. Irwin, *J. Appl. Mech.* **1957**, *24*, 361.
- [24] R. Long, C.-Y. Hui, *Proc. R. Soc. A* **2009**, *465*, 961.